

# An Interpolating Particle Method for the Vlasov–Poisson Equation

R. Paul Wilhlem\*      Matthias Kirchhart†

## Abstract

In this paper we present a novel particle method for the Vlasov–Poisson equation. Unlike in conventional particle methods, the particles are not interpreted as point charges, but as point values of the distribution function. In between the particles, the distribution function is reconstructed using mesh-free interpolation. Our numerical experiments confirm that this approach results in significantly increased accuracy and noise reduction. At the same time, many benefits of the conventional schemes are preserved.

## 1 Introduction

The Vlasov–Poisson system is a simplified model for the evolution of plasmas in their collisionless limit, as they occur in, for example, nuclear fusion devices. In dimensionless form this system is given by:

$$\partial_t f + v \cdot \partial_x f - E \cdot \partial_v f = 0, \quad (1)$$

$$E := -\nabla \varphi, \quad (2)$$

$$-\Delta \varphi = \rho, \quad (3)$$

$$\rho(t, x) := 1 - \int_{\mathbb{R}} f(t, x, v) dv. \quad (4)$$

Here,  $f = f(t, x, v)$  is the electron distribution function, i. e.,  $f(t, x, v)$  describes the probability density of electrons having velocity  $v \in \mathbb{R}$  and location  $x \in \mathbb{R}$  at time  $t \in \mathbb{R}$ . We will assume that  $f$  is periodic in  $x$  with period  $L > 0$ , i. e.,  $f(t, x, v) = f(t, x + kL, v)$  for any  $x \in \mathbb{R}$  and  $k \in \mathbb{Z}$ . Therefore it suffices to look at  $x \in [0, L]$ . We need to demand that  $f$  is normalised such that:

$$\frac{1}{L} \int_{[0, L]} \int_{\mathbb{R}} f(t, x, v) dv dx = 1. \quad (5)$$

Equation (4) defines the charge density  $\rho$ , were the additional ‘1’ stems from the assumption of a uniform ion-background and thus ensures overall neutrality

$$\int_0^L \rho(t, x) dx = 0. \quad (6)$$

Neglecting collisions and the magnetic field, the Vlasov equation (1) then describes the evolution of  $f$  under the influence of the self-consistent electrical field  $E = E(t, x)$ , given in terms of the electric potential  $\varphi = \varphi(t, x)$ , which in turn is given as the solution of the Poisson equation (3).

Particle-in-Cell methods (PIC) are a long established tool to obtain numerical approximations to solutions of this system. However, it is well-known that these methods suffer from ‘numerical noise’ and have a low convergence order.<sup>[1],[2]</sup> For this reason there has been an increased interest in high-order grid-based methods.<sup>[3],[4]</sup> These methods often have good stability properties and generalise to arbitrary order. Unlike

\*Applied and Computational Mathematics, RWTH Aachen University, Schinkelstraße 2, 52062 Aachen, Germany. E-mail: [wilhelm@acom.rwth-aachen.de](mailto:wilhelm@acom.rwth-aachen.de)

†E-Mail: [kirchhart@acom.rwth-aachen.de](mailto:kirchhart@acom.rwth-aachen.de). The second author has been funded by the German Research Foundation (DFG), project number 432219818, ‘Vortex Methods for Incompressible Flows’.

particle methods, however, they introduce numerical dissipation; especially when the true solution develops features that are smaller than the grid size. This is also the case for so-called *remapped* or *remeshed* particle methods: here the particles are periodically remapped onto a Cartesian grid to avoid the aforementioned ‘numerical noise’.<sup>[5]</sup> However, this remeshing effectively acts as a low-pass filter, smearing out features below the grid resolution.

Particle methods without remapping, on the other hand, are based on an analytic solution: particles simply follow the characteristic lines, and are thus free of numerical dissipation. It has recently been shown that the ‘numerical noise’ is actually the result of interpreting the particle field as a quadrature rule.<sup>[6]</sup> Instead of interpreting a particle field as a set of points with associated *weights*, it should be interpreted as a set of points with associated *function values*. Instead of *regularising* a quadrature rule, one should try to *interpolate* between the known function values. In this work we want to show that this in fact leads to particle methods that achieve accuracies comparable to grid-based methods, without the associated introduction of spurious numerical dissipation. Nonetheless, as our numerical experiments will show, aliasing effects limit the accuracy of these approaches, giving rise to phenomena which have not yet been reported for particle methods.

## 2 Related Literature and Methods

The Vlasov–Poisson–Maxwell equations were introduced by Vlasov in his 1938 seminal paper.<sup>[7]</sup> The Vlasov–Poisson system (1)–(4) results when magnetic effects are neglected. In 1945 Landau gave a first analysis of a linearisation of this system close to an equilibrium state.<sup>[8]</sup> Arsen’ev gave the first regularity and well-posedness analysis for the one-dimensional Vlasov–Poisson system.<sup>[9],[10]</sup> Ukai and Okabe extended the results to the two-dimensional case.<sup>[11]</sup> Pfaffelmoser gave an existence and uniqueness result for classical initial data in the three-dimensional case. Lions and Perthame gave an result for weak data.<sup>[12],[13]</sup>

Mouhot and Villani extended the analysis done by Landau to the non-linear system in their seminal paper.<sup>[14]</sup> We refer to their work for more details; it also contains an extensive review of theory, bibliography and historic remarks.

A general overview of numerical methods for the Vlasov–Poisson equation is provided in the books by Birdsall, Langdon and Glassey.<sup>[15],[16]</sup> Filbet and Sonnendrücker compared different Eulerian approaches.<sup>[3],[4]</sup>

Particle methods have their origins in fluid dynamics.<sup>[17],[18],[19]</sup> An introduction to particle methods and their application to the Vlasov–Poisson equation can be found in the articles by Raviart and Cottet<sup>[1],[20]</sup> as well as in Hockney’s book.<sup>[21]</sup>

*Particle-in-Cell* methods (PIC) for the Vlasov–Poisson equation are introduced by Wang, Miller, Colella, Myers and Straalen.<sup>[5],[22]</sup> A more statistical approach to PIC and a combination with Monte-Carlo based methods is presented by Ameres in his recent PhD thesis.<sup>[2]</sup> Ameres also discusses particle noise and its influence on the convergence of (statistical) PIC methods.

Semi-Lagrangian schemes were proposed by Rossmannith and Seal, Sonnendrücker and Besse as well as Charles, Després and Mehrenberger.<sup>[23],[24],[25]</sup>

A general overview of the *reproducing kernel Hilbert space* framework (RKHS) is given in the books by Wendland and Fasshauer.<sup>[26],[27]</sup> For brevity we will refer to methods using the RKHS framework as kernel-based methods. An analysis of the stability of kernel-based interpolation in Sobolev spaces can be found in the article by de Marchi and Schaback<sup>[28]</sup> as well as Rieger’s PhD-thesis.<sup>[29]</sup> The books of Fasshauer and Wendland also give an overview of efficient implementation of techniques for these methods.

Reproducing kernels are used in Eulerian-based approaches for transport equations where this idea was introduced amongst others by Schaback and Franke.<sup>[30]</sup> A kernel-based interpolation approach in the Semi-Lagrangian framework was proposed by Iske and Behrends.<sup>[31]</sup> This ansatz was further developed by several authors for both the linear transport equation and some non-linear equations like the shallow water equation.<sup>[32],[33],[34],[35]</sup>

Finally we want to mention that the RKHS framework was already used in the context of SPH methods. Several authors worked in this context on the so-called RKHS particle method and also applied it to the Vlasov–Poisson equation.<sup>[36]</sup>

### 3 Solution-structure of the Vlasov–Poisson Equation

While in reality the electric field  $E(t, x)$  needs to be computed from the unknown function  $f$  via (2)–(4), let us for the moment assume  $E(t, x)$  was given for all times  $t$ . In this case (1) is a linear transport equation and can be written as

$$\partial_t f(t, z) + (a(t, z) \cdot \nabla_z) f(t, z) = 0,$$

where  $z := (x, v) \in \mathbb{R} \times \mathbb{R}$ ,  $t \geq 0$  and  $a(t, z) := (v, -E(t, x))$ .

This equation can be solved using the method of characteristics. To this end we define the flow-map  $\Phi$  as the solution of the following initial value problem:

$$\frac{d}{dt} \Phi(t; z) = a(t, z) \tag{7}$$

$$\Phi(0; z) = z. \tag{8}$$

Using the flow-map the solution of (1) can be written as

$$f(t, \Phi(t; z)) = f_0(z). \tag{9}$$

Thus, if we track a finite number of ‘particles’  $z_1, \dots, z_N$ , using (7)–(8), we know the value of the solution  $f$  at the current particle positions at any time  $t \geq 0$ , using (9). This is the motivation behind particle methods; they differ in the way how values of  $f$  are obtained in between the particles.

In the one-dimensional case, for classical initial data satisfying a decay condition, Raviart and Cottet have proven, using the work of Ukai and Okabe,<sup>[11]</sup> that (1)–(4) has a unique solution.<sup>[20, Theorem 1]</sup> Thus our initial assumption is justified in the sense that the electric field is indeed well-defined. In a numerical method, the electric field needs to be computed from the current approximation of  $f$ .

### 4 Interpolating Particle Methods

In this section we will first discuss the general structure of interpolating particle methods for the Vlasov–Poisson equation. To this end, we will first give a general algorithm, whose individual steps will be explained in detail in the subsequent subsections.

#### 4.1 Overview

The general structure of interpolating particle methods is as follows:

1. Subdivide the computational domain into a Cartesian grid of widths  $h_x$  and  $h_v$ . Take a sample  $f_i := f_0(x_i, v_i)$ ,  $i = 1, \dots, N$  in each of the grid’s cells. These samples may—but do not need to be—taken at the respective cell centres.
2. Set  $t = 0$ . Enter the time-step loop:
  - a) Compute an interpolant  $f_{h,\sigma}$  on the current set of particles  $(x_i(t), v_i(t))$  and function values  $f_i$ ,  $i = 1, \dots, N$ .
  - b) Compute the charge density:

$$\rho_{h,\sigma}(t, x) := 1 - \int_{\mathbb{R}} f_{h,\sigma}(t, x, v) dv.$$

- c) Solve the Poisson equation for the electric potential:

$$-\Delta \varphi_{h,\sigma} = \rho_{h,\sigma},$$

and define the approximate electric field as  $E_{h,\sigma}(t, x) := -\nabla \varphi_{h,\sigma}(t, x)$ .

- d) Advance the following system of ODEs one step  $\Delta t$  in time, using, e. g., the symplectic Euler method:

$$\begin{cases} \frac{dx_i}{dt}(t) = v_i(t), \\ \frac{dv_i}{dt}(t) = -E_{h,\sigma}(t, x_i(t)), \end{cases} \quad i = 1, \dots, N.$$

Note: For higher order methods, one needs to repeat steps 2a–c for each stage of the Runge–Kutta method to avoid introducing splitting errors.

- e) Set  $t \mapsto t + \Delta t$  and go to [Item 2a](#).

On the one hand, this algorithm closely mirrors conventional blob-based methods. The key difference lies in [Item 2a](#). In a conventional blob method one would chose some blob-function  $\zeta_\sigma(x, v)$  of blob-size  $\sigma > 0$  and set  $f_{h,\sigma} = h_x^d h_v^d \sum_{i=1}^N f_i \zeta_\sigma(x - x_i, v - v_i)$ . The resulting approximation, however, will usually not interpolate the data and contain large errors. If, on the other hand, an appropriate interpolation scheme is employed, drastic improvements in accuracy can be achieved.

## 4.2 Construction of Interpolants

For any given particle field  $(x_i, v_i)$  with associated data  $f_i$ ,  $i = 1, \dots, N$ , there are of course infinitely many possible interpolants. This gives us the freedom to request further conditions. In our case, we demand the following:

- *Accuracy.* The interpolant should converge to the true function  $f$  at high order, i. e., fulfil error bounds of the shape  $\mathcal{O}(h^s)$ , where  $h := \max\{h_x, h_v\}$  is the particle spacing and  $s > 0$  is the (hopefully high) convergence order.
- *Stability.* The interpolant should react gracefully to disturbances in the data  $(x_i, v_i)$  and  $f_i$ ,  $i = 1, \dots, N$ .
- *Efficiency.* Construction and evaluation of interpolants need to be carried out on computers in a fast manner and should require only little extra storage. In particular the algorithm should be easily parallelisable.
- *Ease of integration.* Given an interpolant, it must be possible to compute the charge density  $\rho_{h,\sigma}$  both accurately and efficiently.

These constraints are fulfilled by piece-wise, tensorised kernel-interpolants, which we will describe in more detail.

### 4.2.1 Kernel-based Interpolants

For brevity, we will again use the abbreviation  $z = (x, v) \in \mathbb{R} \times \mathbb{R}$  for coordinates in the phase space. Kernel-based interpolants are functions of the shape  $f_{h,\sigma}(z) = \sum_{i=1}^N c_i k(z, z_i)$ , where  $\mathbf{c} = (c_1, \dots, c_N)^\top \in \mathbb{R}^N$  is a coefficient vector, and  $k(\cdot, \cdot)$  is a suitable kernel function. The coefficient vector needs to be chosen such that the interpolation conditions are fulfilled:

$$\forall i \in \{1, \dots, N\} : f_{h,\sigma}(z_i) = f_i \iff \underbrace{\begin{pmatrix} k(z_1, z_1) & k(z_1, z_2) & \cdots & k(z_1, z_N) \\ k(z_2, z_1) & k(z_2, z_2) & \cdots & k(z_2, z_N) \\ \vdots & \vdots & \ddots & \vdots \\ k(z_N, z_1) & k(z_N, z_2) & \cdots & k(z_N, z_N) \end{pmatrix}}_{=: \mathbf{K}} \underbrace{\begin{pmatrix} c_1 \\ c_2 \\ \vdots \\ c_N \end{pmatrix}}_{=: \mathbf{c}} = \underbrace{\begin{pmatrix} f_1 \\ f_2 \\ \vdots \\ f_N \end{pmatrix}}_{=: \mathbf{f}}. \quad (10)$$

For a given kernel-function  $k$ , the interpolation problem thus reduces to solving the linear system  $\mathbf{Kc} = \mathbf{f}$ , which can be achieved using standard methods.

Classical choices of kernels are radial kernels, i. e.:

$$k(z, \tilde{z}) = b\left(\frac{|z - \tilde{z}|}{\sigma}\right), \quad (11)$$

where  $b : \mathbb{R}_+ \rightarrow \mathbb{R}$  is called the *radial basis function*, and  $\sigma > 0$  is a scaling parameter which needs to be chosen depending on the problem, but *independent of  $h$*  to ensure convergence. Typical choices for  $b$  are Gaussians ( $b(r) = \exp(-r^2)$ ), or Wendland's functions,<sup>[26, Chapter 9]</sup> which are compactly supported piece-wise polynomials. In RKHS literature other often used kernels include inverse multi-quadratics and thin-plate splines. An overview can be found in the books of Wendland and Fasshauer.<sup>[26],[27]</sup> The appropriate choice of kernel depends heavily on the expected solution space. These choices in particular guarantee that the kernel matrix  $\mathbf{K}$  always is symmetric positive definite, such that the system (10) always has a unique solution and can be solved using the Cholesky decomposition.

Note that this approach greatly differs from conventional blob-methods. Superficially, they both use approximations of the shape  $\sum_{i=1}^N c_i k(z, z_i)$ . However, in conventional methods the resulting approximations usually *do not interpolate* the function values  $f_i$ , the coefficient vector *is fixed over time*, the blob width  $\sigma$  *depends on  $h$* , and *no linear system* needs to be solved.

It can be shown that these interpolants have several beneficial mathematical properties, such as minimising the so-called native space norms.<sup>[26, Chapter 10]</sup> For the Wendland kernels the native spaces are isomorphic and norm-equivalent to Sobolev spaces, where the regularity of the Sobolev space depends on the order of the kernel. The norm-minimising property guarantees both accuracy and stability.<sup>[26, Chapters 10–13]</sup> While these interpolants are essentially ideal from the perspective of accuracy and stability, there are practical hurdles to their application in our context:

- Evaluation is costly when the number of particles  $N$  is large. To evaluate  $f_{h,\sigma}$  at a single location  $z$ , it is necessary to perform a summation over all points  $z_i$ ,  $i = 1, \dots, N$ .
- The kernel-matrices  $\mathbf{K}$  are densely populated and tend to be extremely ill-conditioned. This excludes the use of iterative solvers. Especially for Gaussians the matrices quickly become singular within machine precision. This also excludes the use of 'fast algorithms' like multipole methods to speed up evaluation and to avoid explicitly storing  $\mathbf{K}$ .
- Integration along the  $v$ -direction is possible, but difficult.

The first two points are only problematic when using very fine discretisations with large numbers of particles  $N$ . This problem can be alleviated using piece-wise interpolants, as described in [Section 4.2.3](#). Integration becomes significantly easier when one uses tensor-product kernels instead.

#### 4.2.2 Tensorised Kernels

Using the Euclidean distance  $|\cdot|$ , a radial basis function  $b$  can be turned into a kernel in arbitrary high spatial dimensions. An alternative approach is to use tensorised kernels, which result from multiplying low-dimensional kernels, e. g., in our case:

$$k(z, \tilde{z}) = k((x, v), (\tilde{x}, \tilde{v})) = b\left(\frac{|x - \tilde{x}|}{\sigma_x}\right) b\left(\frac{|v - \tilde{v}|}{\sigma_v}\right). \quad (12)$$

Kernels of this form inherit most of the favourable properties of radial kernels. In particular, when choosing the same radial basis function  $b$  as above, they also always result in symmetric positive definite kernel matrices  $\mathbf{K}$ . They give equally high asymptotic convergence orders, albeit with different error constants. The only potential drawback is that now for a single evaluation of  $k$  multiple evaluations of  $b$  are necessary, which is, however, only relevant if  $b$  is expensive to evaluate.

The main benefit in our case is that such interpolants are significantly easier to integrate along a single coordinate axis. Assume we are given an interpolant  $f_{h,\sigma}(z) = \sum_{i=1}^N c_i k(z, z_i)$  with a tensorised kernel  $k$ . We then can compute the charge density  $\rho_{h,\sigma}$  as follows:

$$\rho_{h,\sigma}(x) = 1 - \int_{-\infty}^{\infty} f_{h,\sigma} dv = 1 - \sum_{i=1}^N c_i b\left(\frac{|x - x_i|}{\sigma_x}\right) \underbrace{\int_{-\infty}^{\infty} b\left(\frac{|v - v_i|}{\sigma_v}\right) dv}_{:=\Lambda}, \quad (13)$$

where the last integral is a constant that only depends on  $b$  and  $\sigma_v$ . Once this constant has been computed, evaluation of  $\rho_{h,\sigma}$  then reduces to computing the sum and the evaluation of  $b$ . In the case of Wendland's functions,  $b$  is a piece-wise polynomial and the integral can be easily evaluated analytically.

### 4.2.3 Piece-wise Interpolants

In case of the Vlasov–Poisson equation, only integrals along the  $v$ -direction of  $f$  are taken. In particular, no derivatives or point evaluations of  $f$  are required. It is thus not necessary to construct a globally smooth interpolant  $f_{h,\sigma}$ . This justifies the use of piece-wise interpolants: the computational domain is divided into a disjoint union of axis-aligned boxes, each of which containing only a small number of particles (usually about 200 for the one-dimensional case). Then in each of these boxes a local, kernel-based interpolant is computed. This way, the size of the kernel-system (10) remains bounded: instead of solving one large system of dimension  $\mathbb{R}^{N \times N}$ , we now solve many small systems of dimension  $\mathbb{R}^{N_{\text{box}} \times N_{\text{box}}}$ . As the number of particles in an individual box  $N_{\text{box}}$  is bounded by a user-defined constant, the cost for solving this local system remains constant as well. Thus, solving all of these local systems separately, one ends up with an overall optimal complexity of  $\mathcal{O}(N)$ . The subdivision of the domain into boxes can efficiently be achieved using *kd*-trees.<sup>[26, Chapter 12.4]</sup> In this work we use the cyclic splitting rule.

The integration of the resulting interpolant  $f_{h,\sigma}$  along the  $v$ -axis gets only slightly more complicated. Suppose we are given a finite set of locations  $x^1, x^2, x^3, \dots, x^{N_\rho}$  at which we want to evaluate  $\rho_{h,\sigma} = 1 - \int f dv$ . We use superscripts to distinguish these points from the particle locations  $z_i = (x_i, v_i)$ ,  $i = 1, \dots, N$ . This evaluation can be achieved using the following algorithm:

1. For  $i = 1, \dots, N_\rho$  set  $\rho_{h,\sigma}^i \leftarrow 1$ .
2. For each box  $B$  of the piece-wise interpolant  $f_{h,\sigma}$ :
  - a) Find the evaluation points  $x^i$  with  $\{x^i\} \times \mathbb{R} \cap B \neq \emptyset$ .
  - b) For each such point  $x^i$  set:

$$\rho_{h,\sigma}^i \leftarrow \rho_{h,\sigma}^i - \int_{v_{\min}(B)}^{v_{\max}(B)} f_{h,\sigma}(x^i, v) dv.$$

Here  $v_{\min}(B)$  and  $v_{\max}(B)$  denote the respective minimum and maximum  $v$  coordinates of the axis-aligned box  $B$ . The last integral can be evaluated exactly when using tensorised kernels and the ordinary anti-derivative  $\mathfrak{b}, \mathfrak{b}' = b$  of the radial function  $b$  is known. This is the case for the Wendland functions, which are piece-wise polynomials. Thus, in this case, integration can be carried out efficiently and exactly. We also remark that this algorithm can be efficiently parallelised.

In the remainder of the paper, when using piece-wise interpolants, we will refer to this as the piece-wise method or the PW method; in contrast, when using global kernel interpolants we will use the term 'direct method'.

## 4.3 Computation of the Electric field

Given the numerical approximation  $\rho_{h,\sigma}$ , one needs to solve the Poisson equation with periodic boundary conditions to obtain  $E_{h,\sigma}$ , i. e., one has to solve:

$$-\Delta \varphi_{h,\sigma} = \rho_{h,\sigma} \tag{14}$$

$$\varphi_{h,\sigma}(0) = \varphi_{h,\sigma}(L) = 0. \tag{15}$$

From this one can compute  $E_{h,\sigma} = -\nabla_x \varphi_{h,\sigma}$ .

In this work we use a standard Galerkin method and periodic B-Splines of order 8 and high spatial resolution for this problem.

Alternatively it is possible to exploit the solution structure of  $f_{h,\sigma}$  and  $\rho_{h,\sigma}$ , when using tensorised Wendland-kernels. For the 1d Poisson equation with periodic boundary conditions the Green's function  $G(x, y)$  and its derivative  $K(x, y)$  are explicitly known,<sup>[20]</sup> such that we can write

$$E_{h,\sigma}(x) = \int_0^L K(x, y) \rho_{h,\sigma}(y) dy. \tag{16}$$

Now, using (13), the above equation turns into

$$E_{h,\sigma}(x) = \int_0^L K(x,y)dy - \Lambda \sum_{i=1}^N c_i \int_0^L K(x,y)b\left(\frac{|x-x_i|}{\sigma_x}\right) dy. \quad (17)$$

Both integrals can be evaluated analytically using that Wendland-kernels are essentially polynomials.

This yields a speed-up for the Poisson solver step, however, our benchmarks showed that the interpolation process to obtain  $f_{h,\sigma}$  takes several times more computation time than solving for the electric field  $E_{h,\sigma}$ , even when going to very high resolution in the numerical Poisson solver. We therefore decided against implementing equation (17).

## 5 Elements of a Convergence Analysis

In the following we will sketch a proof for the theoretic convergence order of our method. To this end we will restrict ourselves to the linear case, i. e., where the electric field, and therefore the velocity field  $a(t, \cdot)$ , is assumed to be known at all times  $t$ . Furthermore we will neglect the time-integration error when solving (7)–(8) numerically and restrict ourselves to radial-basis instead of tensorised kernels. We expect similar results to hold for both types of kernels and numerical experiments support this hypothesis as well. However, their respective native spaces would differ slightly, thus we would need to give a technical and lengthy derivation of the correct estimates. We only consider the direct method. The related convergence result for the piecewise method can be proven analogously when interpreting the piecewise interpolant as a approximation of the global interpolant, thus having locally the same convergence order.

**Theorem (Convergence linear case).** *Let  $f_0$  be smooth enough and periodic in the first component with period  $L > 0$ . Furthermore let  $f_0$  satisfy*

$$\forall x, v \in \mathbb{R} : f_0(x, v) \geq 0, \quad (18)$$

$$\exists v_{\max} > 0 \forall x \in \mathbb{R}, |v| \geq v_{\max} : f_0(x, v) = 0, \text{ and} \quad (19)$$

$$\frac{1}{L} \int_0^L \int_{-\infty}^{\infty} f_0(x, v) dv dx = 1. \quad (20)$$

Assume that the solution  $E$  to (2)–(4) is known in advance.

Let  $Z_0 \subset Q := [0, L] \times [-v_{\max}, v_{\max}]$  be a finite set of distinct particles,  $|Z_0| = N$ , such that the fill distance fulfils

$$h := \sup_{z \in Q} \inf_{s \in Z_0} |z - s| \in (0, \chi), \quad (21)$$

where the constant  $\chi := \chi(Q)$  is defined in Wendland's book and depends on the volume and geometry of the domain  $Q$ .<sup>[26, Theorem 11.32]</sup> We choose  $b$  to be a Wendland kernel of high enough order such that  $N_b(Q) \subset H^m(Q)$ . Without loss of generality assume  $\sigma = 1$ .

The numerical solution  $f_{h,\sigma}$ , is reconstructed via (10) using the exact positions  $Z(t) := \{z_i(t)\}_{i=1}^N$  and function values  $\{f_1, \dots, f_N\}$ , from solving (7)–(8). Then  $f_{h,\sigma}$  satisfies the error bound

$$\|f(t) - f_{h,\sigma}(t)\|_{L^p(Q)} \leq Ch^{m-l(p)} \|f_0\|_{H^m(Q)}, \quad (22)$$

where  $C > 0$  depends on  $t$  and additionally the volume of  $Q$ , i. e.,  $v_{\max}$  and  $L$ , if  $p = 1, 2$ . The constant  $l := l(p)$  is defined as

$$l(p) = \begin{cases} 2\left(\frac{1}{2} - \frac{1}{p}\right) & p \geq 2 \\ 0 & p = 1 \end{cases}.$$

*Proof.* Let  $t \geq 0$  be a fixed time and the exact solution of (7)–(8) with the starting positions  $Z(0) = Z_0$ . Furthermore assume that the particle positions  $Z(t)$  are mapped back to their periodically equivalent positions in  $Q$  at time  $t$ , i. e.,  $Z(t) \subset Q$  without loss of generality.

From [Section 3](#) we know that  $f(t, \cdot, \cdot)$  has the same regularity as  $f_0$ . Thus, using standard estimates we have:<sup>[26, Corollary 11.33]</sup>

$$\exists C > 0 : \|f(t) - f_{h,\sigma}(t)\|_{L^p(Q)} \leq Ch_{Z(t),Q}^{m-l(p)} \|f(t)\|_{H^m(Q)}, \quad (23)$$

where  $C$  does depend on  $Q$  as stated in above theorem. Using (9), and the Hölder inequality one obtains

$$\|f(t)\|_{H^m(Q)} = \|f_0 \circ \Phi_t^0\|_{H^m(Q)} \leq \underbrace{\|\Phi_t^0\|_{H^m(Q)}}_{c:=} \|f_0\|_{H^m(Q)}. \quad (24)$$

The constant  $c$  depends on the problem, but is independent of the discretisation and thus:

$$\exists C > 0 : \|f(t) - f_{h,\sigma}(t)\|_{L^p(Q)} \leq Ch_{Z(t),Q}^{m-l(p)} \|f_0\|_{H^m(Q)}, \quad (25)$$

holds with  $h_{Z(t),Q}$  is the fill distance of  $Z(t)$ .<sup>[20, section 1]</sup>

Finally, using that  $\|\nabla\Phi\|_{L^\infty}$  is bounded for finite time-intervals, one obtains

$$h_{Z(t),\Omega} \leq \tilde{C}h, \quad (26)$$

where the constant  $\tilde{C} > 0$  depends on  $t$ .<sup>[20, Lemma 3-5]</sup> This concludes the proof.  $\square$

Our numerical experiments indicate that high orders of convergence are preserved in the non-linear setting. A complete proof is beyond the scope of this work.

## 6 Numerical results

We consider three standard benchmarks: *weak linear Landau damping*, *two stream instability* and *bump on tail instability*. For the interpolation step we used both the direct and piece-wise ansatz (PW), depending on the number of particles. Piece-wise interpolants tend to develop overshoots near the boundaries of the respective boxes, but can be efficiently computed for large numbers of particles. Direct kernel-interpolants use the entire set of particles at once and therefore do not suffer from this problem. This, however, comes at the price of an  $O(N^3)$  complexity and for this reason the direct approach does not scale well to large numbers of particles. We will carry out experiments using both approaches to assess whether the increased accuracy of the direct ansatz outweighs its cost.

Tensorised Wendland kernels were used for all interpolations. In the following we will only specify the order of the kernel in use.

Preliminary experiments have shown that for our test cases reasonable ranges for the scaling parameters are  $1 \leq \sigma_x, \sigma_v \leq 6$ . For the finest discretisations the resulting kernel matrices became too ill-conditioned even for direct linear solvers. For this reason we apply Tikhonov regularisation and solve the modified systems  $(K + \mu^2 I) c = f$  with regularisation parameter  $\mu = 10^{-5}$ . For the phase-space sub-division we use  $N_{box} = 200$ .

### 6.1 Weak Landau damping

The initial condition is

$$f_0(x, v) := \frac{1}{\sqrt{2\pi}} e^{-\frac{v^2}{2}} (1 + \alpha \cos(kx)), \quad (x, v) \in [0, L] \times \mathbb{R} \quad (27)$$

with  $k = 0.5$ ,  $\alpha = 0.01$ ,  $L = 4\pi$ . The velocity space is cut at  $v_{\max} = 6$ . The initial state (27) is a small perturbation to the Maxwellian distribution

$$f_M(v) = \frac{1}{\sqrt{2\pi}} e^{-\frac{v^2}{2}},$$

which is a steady state solution of the Vlasov–Poisson equation (1). For the direct method we used  $h_x = \frac{L}{32}$  and  $h_v = \frac{v_{\max}}{32}$ , while for the PW ansatz  $h_x = \frac{L}{512}$  and  $h_v = \frac{v_{\max}}{512}$  were used. The scaling parameters were

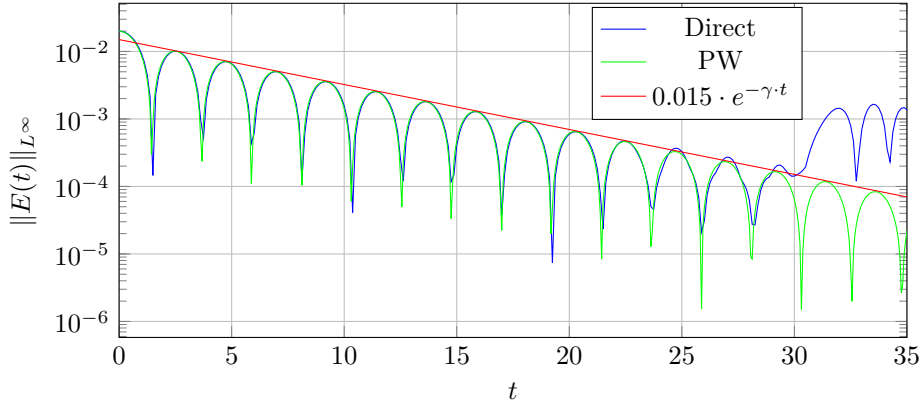


Figure 1: *Electric field amplitude for the weak Landau damping benchmark. The direct method (blue graph) uses  $h_x = \frac{L}{32}$ ,  $h_v = \frac{v_{\max}}{32}$ ,  $\Delta t = \frac{1}{8}$ , fourth order classical Runge-Kutta method and second order kernels. The PW method (green graph) uses  $h_x = \frac{L}{512}$ ,  $h_v = \frac{v_{\max}}{512}$ ,  $dt = \frac{1}{16}$ , symplectic Euler and second order kernels. Up to  $t = 25$  the numerical damping rate of both methods are in good agreement with the theoretical prediction. At  $t \approx 29$  the recurrence effect sets in for the direct method, and between  $t = 24$  and  $29$  the amplitude maxima are slightly overshooting their theoretical value. The PW method, on the other hand, reproduces the correct damping behaviour until  $t = 35$ .*

chosen as  $\sigma_x = 3$ ,  $\sigma_v = 1$  for the direct method and  $\sigma_x = 6$ ,  $\sigma_v = 3$  for the PW method. We used second order kernels for both methods. For time-integration we used the classical Runge-Kutta method with  $\Delta t = \frac{1}{8}$  for the direct method and a symplectic Euler scheme with  $\Delta t = \frac{1}{16}$  for the PW method. We chose a low order time-integration method for the PW ansatz as the reconstructed solution is only piecewise continuous. Note that while larger time-steps would be possible due to the lack of a CFL-condition, we opted for smaller time-steps to better resolve the evolution of the electric field amplitude when plotting.

Figure 1 shows the evolution of the electric field amplitude over time. From theory and numerical experiments we know that the electric field will get damped periodically at rate  $\gamma = 0.153359$  and oscillation frequency  $\omega = 1.41566$ .<sup>[37]</sup> Until  $t \approx 25$  both methods are in good agreement with theory. At this point we observe a recurrence phenomenon for the direct approach: the electric field amplitude increases again and a new damping process begins. This is remarkable as recurrence has been known for grid-based solvers,<sup>[38]</sup> but it has been claimed that particle methods do not suffer from this effect.<sup>[39]</sup> Conventional blob methods, however, become ‘noisy’ at this stage, and we believe that it is this noise that masks the recurrence.<sup>[2],[5],[22]</sup>

The cause of this phenomenon can be seen in Figure 2, which shows the evolution of the difference between the numerical solution  $f_{h,\sigma}$  and the Maxwellian distribution  $f_M$ . One can observe waves of increasing frequency entering the domain from  $v \rightarrow \pm\infty$ . Starting at  $t = 30$ , unphysical artefacts appear in the plot of the direct method. At this point we can observe an aliasing effect: the high-frequency modes are not correctly captured by the low resolution of the direct method. The higher resolution of the PW method, however, can correctly reproduce  $f$  for extended period of times.

In the limit  $t \rightarrow +\infty$  and for the initial datum (27) the analytic solution  $f(t, \cdot, \cdot)$  will weakly converge to a steady state but not in a strong sense.<sup>[14]</sup> The solution  $f$  develops waves of increasing frequency and number with time and therefore develops a small scale structure. Thus the PW method will eventually suffer from recurrence as well.

## 6.2 Two stream instability

For our second benchmark we consider the initial condition

$$f_0(x, v) = \frac{1}{\sqrt{2\pi}} v^2 e^{-\frac{v^2}{2}} (1 + \alpha \cos(kx)), \quad (x, v) \in [0, L] \times \mathbb{R} \quad (28)$$

with  $\alpha = 0.01$ ,  $k = 0.5$ ,  $L = 4\pi$ . We use  $v_{\max} = 8$  as cut-off in velocity-space. The *two stream instability* simulates two particle streams of same density but opposing velocities colliding with each other. The initial

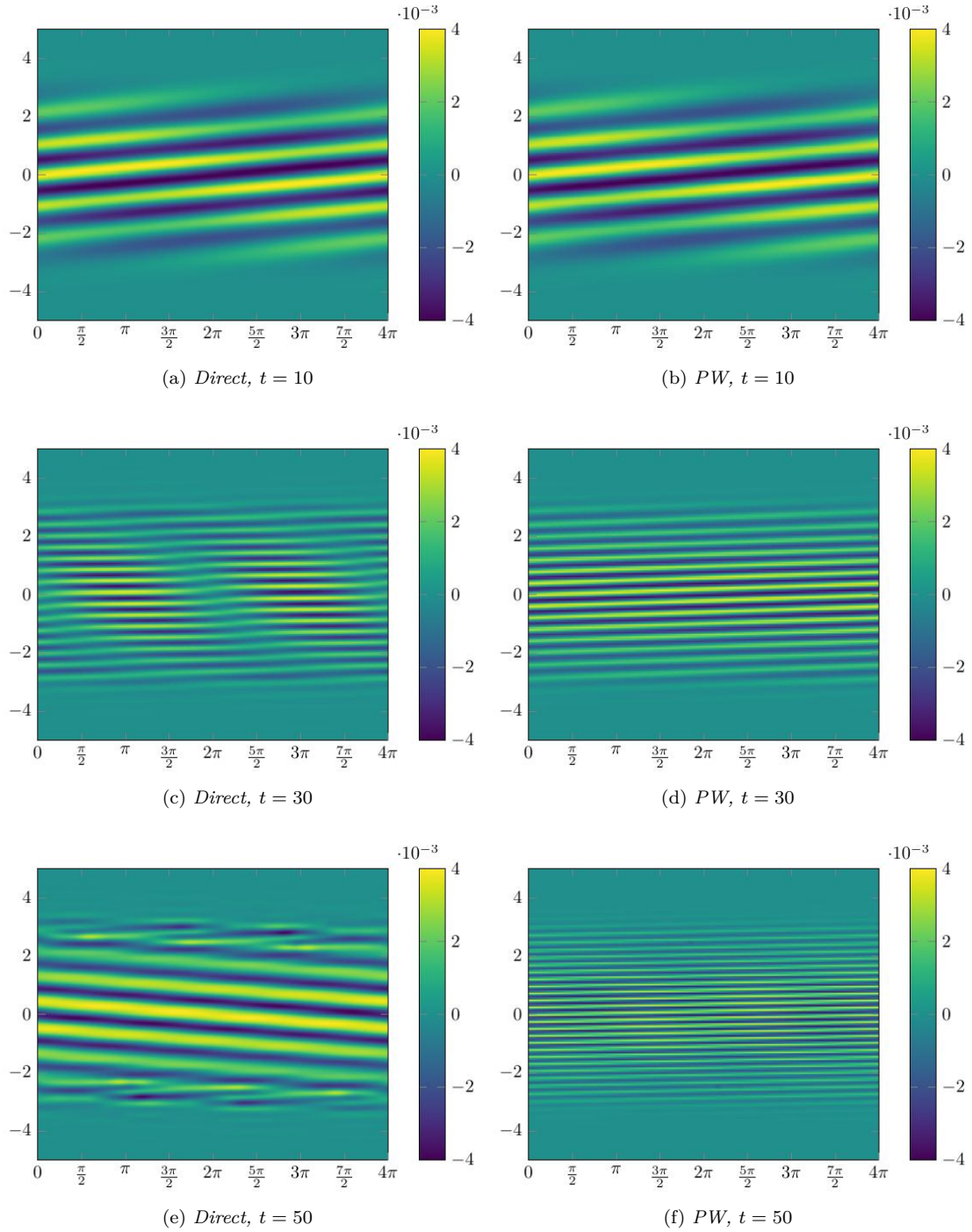


Figure 2: Difference between the numerical solution  $f_{h,\sigma}$  and the Maxwellian equilibrium  $f_M$  for the weak Landau damping benchmark. On the left-hand-side  $f_{h,\sigma}$  is computed via the direct method and on the right-hand-side using the PW method. The resolutions are the same as in Figure 1. For  $t \leq 30$  the number of waves is steadily increasing. For the lower resolution, starting at  $t = 30$ , numerical artefacts can be observed. At  $t = 50$  aliasing occurs: the spatial resolution is insufficient to capture the highest frequencies. Therefore high frequencies appear as low ones. The high-resolution solution can resolve the solution correctly up to  $t = 50$ .

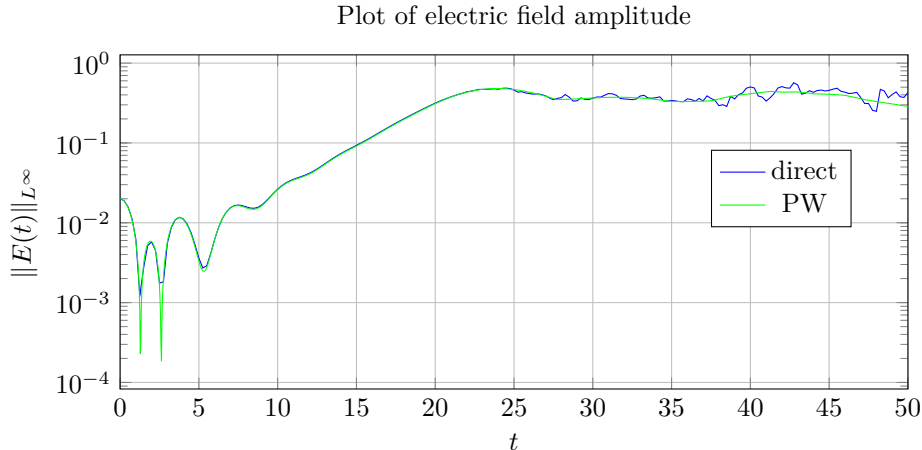


Figure 3: *Electric field amplitude for the two stream instability. The direct method (blue) used  $h_x = \frac{L}{64}$ ,  $h_v = \frac{10}{128}$ ,  $\Delta t = \frac{1}{4}$  and the classical Runge-Kutta method. The PW method (green) used  $h_x = \frac{L}{512}$ ,  $\frac{10}{1024}$ ,  $\Delta t = \frac{1}{32}$  and the symplectic Euler method. Both the direct and PW method employed fourth order kernels. After an initial damping until  $t \approx 5$  the mixing process starts dominating the dynamics. The electric field amplitude arrives at its maximum at approximately  $t \approx 23$  and starts periodically oscillating afterwards. Until  $t \approx 23$  the increase of amplitude is captured correctly by both methods. After  $t \approx 25$  slight numerical artefacts appear in the solution computed with lower resolution.*

state is a slight perturbation of the unstable equilibrium

$$f_{eq}(v) = \frac{1}{\sqrt{2\pi}} v^2 e^{-\frac{v^2}{2}}.$$

We used  $h_x = \frac{L}{64}$  and  $h_v = \frac{v_{\max}}{128}$  for the direct method and  $h_x = \frac{L}{512}$  and  $h_v = \frac{v_{\max}}{1024}$  for the PW method. The scaling parameters were fixed as  $\sigma_x = 2$ ,  $\sigma_v = 1$  for the direct method and  $\sigma_x = 4$ ,  $\sigma_v = 2$  for the PW method. For both methods we used fourth order kernels. The time-steps are set to  $\Delta t = \frac{1}{4}$  and  $\Delta t = \frac{1}{32}$  with classical Runge-Kutta and symplectic Euler as time-integrators respectively.

The evolution of the electric field's amplitude is depicted in [Figure 3](#). Because the direct approach is limited to fairly small numbers of particles, i. e., coarse resolutions, it performs worse than the PW method. However, the direct method is still able to capture the dynamics of both  $f$  and  $E$  qualitatively correctly. The forming of the filaments introduces steep gradients. This results in overshoots in the numerical solution, as soon as these gradients can no longer be resolved by the fixed resolution.

This can clearly be observed in [Figure 4](#) after  $t \approx 30$  in the plots for the direct method. While the direct and PW methods, similar to grid-based methods, suffer from overshoots and thus do not provide good accuracy for extended times in turbulent simulations, they reproduce the fine details of  $f$  better than Eulerian or PIC methods.

### 6.3 Bump on tail instability

The initial condition for our final benchmark, the *bump on tail instability*, is

$$f_0(x, v) = \frac{1}{\sqrt{2\pi}} \left( n_p \cdot e^{-\frac{v^2}{2}} + n_b \cdot e^{-\frac{1}{2} \frac{(v-v_b)^2}{v_t^2}} \right) (1 + \alpha \cos(kx)). \quad (29)$$

with  $n_p = 0.9$ ,  $n_b = 0.2$ ,  $v_b = 4.5$ ,  $v_t = 0.5$ ,  $\alpha = 0.04$ ,  $k = 0.3$ ,  $L = \frac{2\pi}{0.3}$ .<sup>[37]</sup> The cut-off in velocity space is set to  $v_{\max} = 10$ . For this test case we only consider the PW method and are interested in both long- and short-term accuracy. We chose  $h_x = \frac{L}{1024}$  and  $h_v = \frac{v_{\max}}{512}$  as resolution and second order kernels. The scaling parameters were set to  $\sigma_x = 6$ ,  $\sigma_v = 3$ . The time-step is set to  $\Delta t = \frac{1}{16}$  and the symplectic Euler time integration method was used.

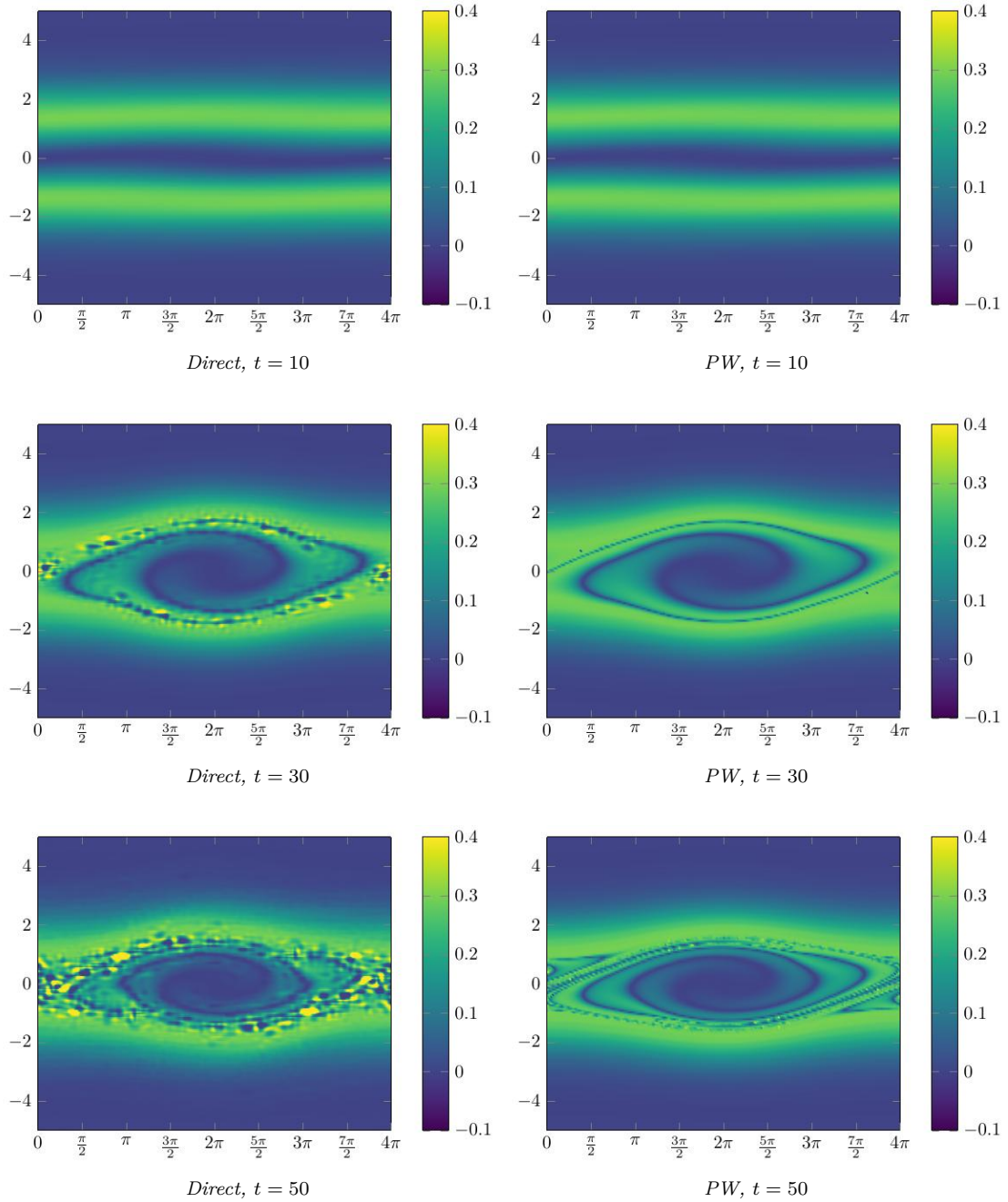


Figure 4: The distribution function  $f_{h,\sigma}(t, x, v)$  for the two stream instability benchmark. The numerical solution computed using the direct method is on the left-hand side, the PW method on the right-hand side. The parameters were chosen as in Figure 3. At  $t \approx 10$  the phase-space ‘vortex’ starts to form. After  $t = 30$  one can observe the ‘vortex’ rotation. With each rotation further filaments enter the ‘vortex’. It can also be observed that the filaments enter at  $x = 0$  or  $x = 4\pi$  and drift towards the center of the ‘vortex’. While both methods reproduce the dynamics of  $f$  qualitatively correct, the errors made by the direct method are significantly higher. Both methods suffer from overshoots near filaments.

The *bump on tail instability* simulates the clash of a low density particle stream with Maxwellian velocity distribution around  $v_b = 4.5$  into resting particles, i. e., with Maxwellian velocity distribution around 0. The equilibrium state

$$f_{eq}(v) = \frac{1}{\sqrt{2\pi}} \left( n_p \cdot e^{-\frac{v^2}{2}} + n_b \cdot e^{-\frac{1}{2} \frac{(v-v_b)^2}{v_t^2}} \right)$$

gets slightly perturbed, whereby the mixing process is initiated. The resulting dynamics can be described as an overlapping of the effects of *weak Landau damping* and the *two stream instability*, i. e., an overlapping of mixing and damping processes. Which effect dominates, depends on the difference in density and the strength of the initial perturbation.

For the chosen set of parameters, the damping effect on electric field is small and only becomes apparent at large time intervals. Therefore the benchmark involves being able to simulate the correct behaviour for times  $t \gg 100$ . In [Figure 5](#) one sees the long time damping, which is in good agreement with the results presented by Arber and Vann.<sup>[37]</sup>

In [Figure 6](#) we see an initial damping between  $t = 0$  and  $t \approx 5$ . On the one hand, after  $t \approx 5$  a ‘vortex’ begins to form that will eventually dominate the dynamics for early times. The ‘vortex’ moves periodically in phase space along the  $x$ -axis. This can be seen in [Figure 8](#). After  $t \approx 20$  an increase in the number of filaments can be observed. This effect is similar to that of [Figure 4](#) from the *two stream instability* simulation.

On the other hand, starting at  $t \approx 20$  one can observe waves forming on the particle cluster centred at  $v = 0$ . This is comparable to *weak linear Landau damping*, see [Figure 2](#). Note, that compared to the previous two benchmarks, the perturbation strength  $\alpha = 0.04$  is significantly higher and thus the amplitudes of appearing waves are higher as well.

Similar to the *two stream instability* benchmark, we observe overshoots resulting in slight numerical noise in this simulation, see [Figures 8e](#) and [8f](#). But in contrast to the *two stream instability* benchmark, the gradients do not get as steep and therefore the simulation stays stable even with fewer particles and for extended periods of time.

## 6.4 Convergence study

In this section we investigate the convergence behaviour of the PW method in the setting of the *weak Landau damping* benchmark. To this end [Figure 7](#) displays the  $L^\infty$ -errors with increasing resolution. The results are compared against results of a computation with very high resolution.

From [Section 5](#) we expect a convergence in the order of  $O(h^2)$  for  $h \rightarrow 0$ . For times  $t < 15$  this prediction is being supported by the graph. In fact after cutting  $h$  in half, the error is reduced by a factor of approximately 0.1. This corresponds to an empirical convergence rate of more than 3, thereby *exceeding the predictions*.

With time, the increasing filamentation causes increasingly steep gradients in the solutions, thereby reducing its smoothness from a numerical perspective. In particular this leads to higher native space norms – these can be estimated using  $H^m$ -norms – and therefore the error constant increases as well. This explains the increasing errors observed after  $t \approx 15$ .

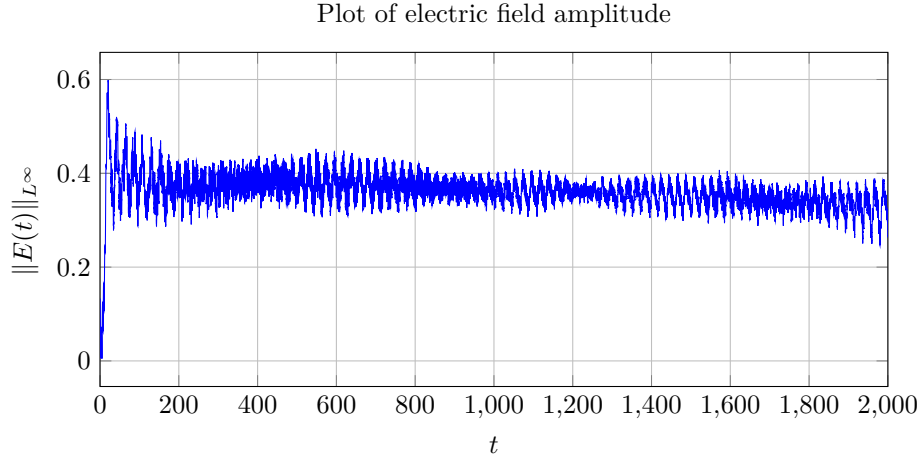


Figure 5: Amplitude of the electric field until  $T = 2000$  for the bump on tail instability benchmark. The simulation was run at resolution  $h_x = \frac{L}{1024}$ ,  $h_v = \frac{10}{512}$  and time step  $\Delta t = \frac{1}{16}$  using the symplectic Euler method. After an initial increase of amplitude, several oscillation modes can be observed. In the long time limit  $t \rightarrow 2000$  the amplitude gets gradually damped.

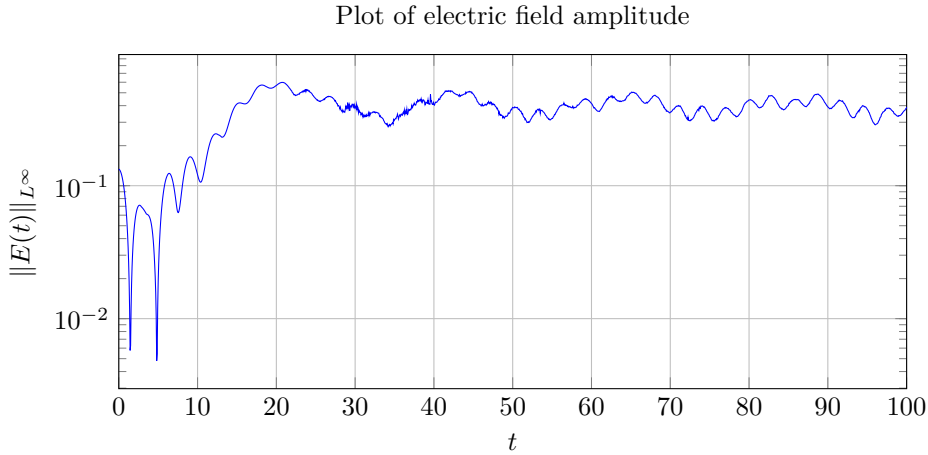


Figure 6: Amplitude of the electric field of the bump on tail instability until  $T = 50$  with simulation parameters as in figure [Figure 5](#). After an initial damping until  $t \approx 5$  the amplitude increases to reach its global maximum at  $t \approx 20$ . Then there are two dominating oscillation modes, a slow oscillation with period  $\approx 22$  and another faster oscillation with period  $\approx 2.5$ . The first oscillation is caused by the mixing of the two particle streams, see [Figure 3](#), the second oscillation is caused by a Landau damping effect, see [Figure 1](#). Between  $t = 30$  and  $t = 40$  one can observe numerical noise. At this point the mixing of the two streams is causing steep gradients and thus overshoots in the numerical solution  $f_{h,\sigma}$  which results in numerical errors when computing  $E_{h,\sigma}$ . After  $t = 50$ , the amplitude is reproduced correctly again.

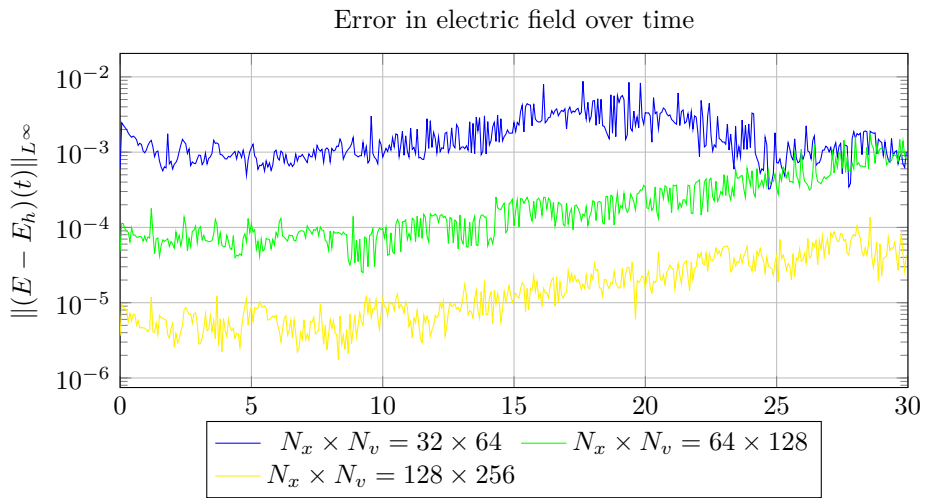


Figure 7:  $L^\infty$ -errors of the electric field for three different resolutions for the weak linear Landau Damping benchmark. We used the PW ansatz with second order kernels and  $\Delta t = \frac{1}{16}$  as time-step for simulations. As a reference a computation with  $h_x = \frac{L}{512}$  and  $h_v = \frac{10}{1024}$  was used. For  $t \in [0, 15]$  the errors stay approximately constant. After  $t > 15$  the errors of approximations computed with higher resolutions slowly increase by one order of magnitude until  $t \approx 30$  while the error of the lowest resolution computation drops again after an initial increase. This seems to be a numerical artefact.

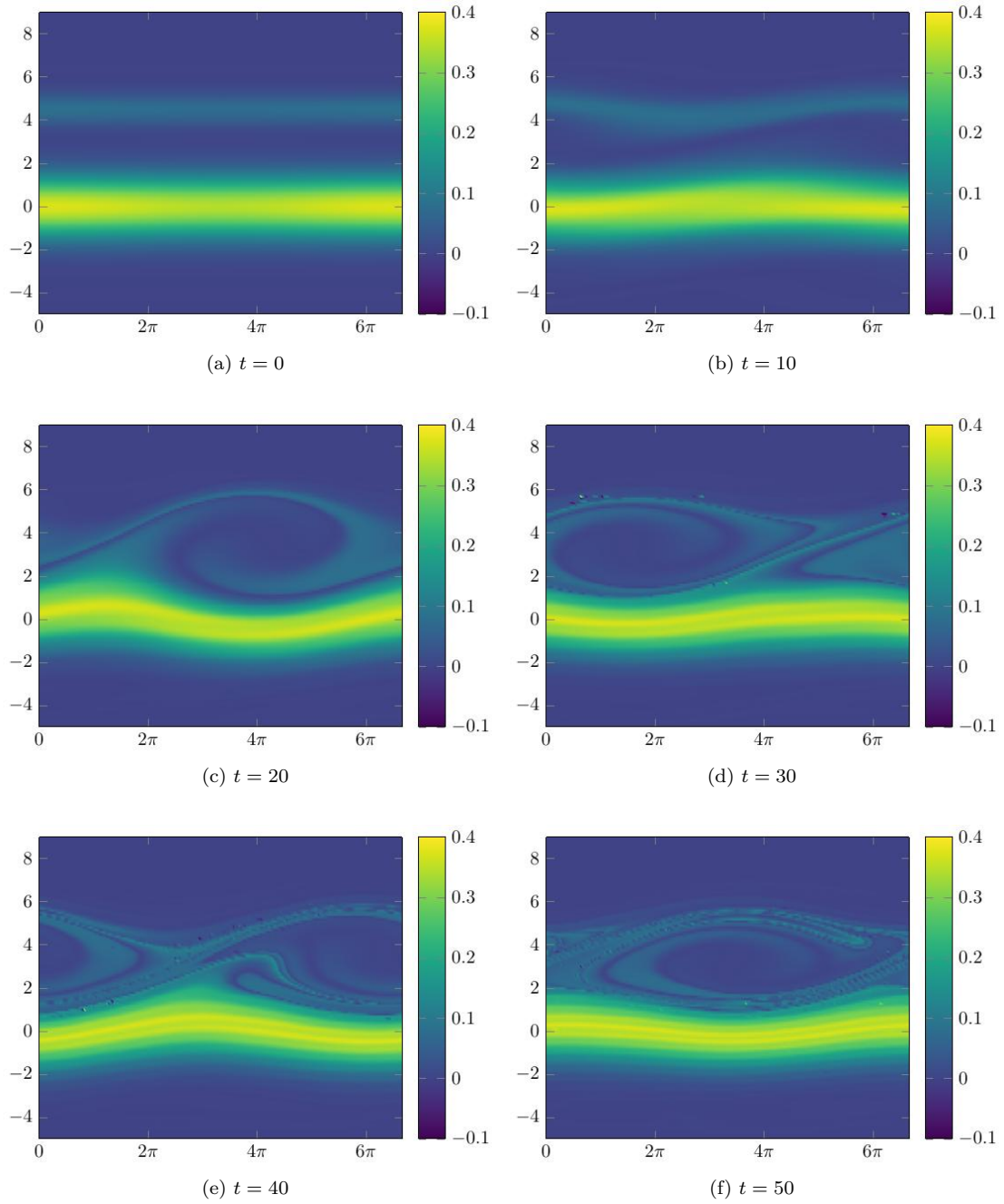


Figure 8: Evolution of the distribution function  $f_{h,\sigma}(t, x, v)$  until  $T = 50$  for the bump on tail instability. Computed using the PW method with the same parameters as in Figure 5. Beginning at  $t \approx 10$  the phase-space ‘vortex’ starts to form and gets fully developed at  $t \approx 20$ . Afterwards it starts periodically moving along the  $x$ -axis with a period of  $\approx 22$  which coincides with the slow oscillation in Figure 6. After  $t = 20$  the formation of so-called Langmuir waves on the bigger particle cluster can be observed. This coincides with the faster oscillations appearing in Figure 6 with period  $\approx 2.5$ .

## 7 Conclusion

We have presented a particle method using meshfree interpolation of arbitrary high order and investigated numerically, whether the good convergence behaviour from RKHS theory carries over to the case of the fully non-linear Vlasov-Poisson equation in the  $d = 1$  case.

In contrast to conventional particle methods like PIC or SPH, our method does not need a remapping strategy to avoid numerical noise. Furthermore, as interpolation with Wendland-kernels is stable with arbitrary high convergence order, our method needs significantly fewer particles to achieve the same accuracy as classical particle methods. The downside is that our method struggles with steep gradients, which naturally appear in solutions of the Vlasov-Poisson equation. To resolve them correctly, any interpolation method needs high resolution, irrespective of the convergence order of the method. Similar problems can be observed with higher order Eulerian Vlasov solvers. Steep gradients lead to overshoots in the numerical solution, which violate the positivity and  $f(t, x, v) \leq \|f_0\|_{L^\infty}$  constraints, making the solution unphysical. Thus, the straight-forward use of high-order kernels only has a positive impact on accuracy with high enough resolutions in comparison to lower-order kernels.

The ill-conditioning of the kernel matrices is a well-known problem and its solution is an ongoing research topic in the RKHS community. This limits the particle numbers for the direct method. In case of the Vlasov-Poisson equation, however, this problem can be bypassed by using piece-wise interpolants instead. Our simulations have illustrated that this approach does in fact result in efficient and high order accurate schemes.

To summarise, the presented particle method offers a good compromise between the stability and high accuracy of purely Eulerian methods on the one hand and speed and hyperbolicity of classical particle methods on the other hand, while avoiding the inherent numerical noise of the latter. RKHS-theory offers a straight-forward interpolation scheme which does not depend on the dimension and of the underlying problem and thus is well-suited for an extension to the  $d = 2, 3$  cases of the Vlasov-Poisson equation.

In the future we plan on extending our scheme to the higher dimensional cases of the Vlasov-Poisson equation. To this end we are also trying to further address the ill-conditioning with methods like multigrid-interpolation or approximate cardinal functions. Furthermore, we are looking at ways to reliably resolve the steep gradients, by, e.g., adding further particles in time where filaments appear.

## References

- [1] P. Raviart. ‘An analysis of particle methods’. In: *Numerical Methods in Fluid Dynamics* (1985), pp. 243–324. DOI: [10.1007/BFb0074532](https://doi.org/10.1007/BFb0074532).
- [2] J. Ameres. ‘Stochastic and Spectral Particle Methods for Plasma Physics’. PhD thesis. Technische Universität München, 2018.
- [3] F. Filbet and E. Sonnendrücker. ‘Comparison of Eulerian Vlasov Solvers’. In: *Computer Physics Communications* 150.3 (July 2001), pp. 247–266. ISSN: 0010-4655. DOI: [10.1016/S0010-4655\(02\)00694-X](https://doi.org/10.1016/S0010-4655(02)00694-X).
- [4] F. Filbet, E. Sonnendrücker and P. Bertrand. ‘Conservative Numerical Schemes for the Vlasov Equation’. In: *Journal of Computational Physics* 172.1 (Sept. 2001), pp. 166–187. ISSN: 0021-9991. DOI: [10.1006/jcph.2001.6818](https://doi.org/10.1006/jcph.2001.6818).
- [5] B. Wang, G. H. Miller and P. Colella. ‘A Particle-in-cell Method with Adaptive Phase-space Remapping for Kinetic Plasmas’. In: *SIAM J. Sci. Comput.* 33.6 (Dec. 2011), pp. 3509–3537. DOI: [10.1137/100811805](https://doi.org/10.1137/100811805).
- [6] M. Kirchhart and C. Rieger. ‘Discrete Projections: A Step Towards Particle Methods on Bounded Domains without Remeshing’. In: *SIAM Journal on Scientific Computing* 43.1 (Feb. 2021), A609–A635. ISSN: 1064-8275. DOI: [10.1137/19M1299864](https://doi.org/10.1137/19M1299864).
- [7] A. Vlasov. ‘On the vibrational properties of an electronic gas’. In: *Zh. Eksp. Teor. Fi.* 8, 291 (1938).
- [8] L. Landau. ‘On the Vibrations of the Electronic Plasma’. In: *Collected Papers of L.D. Landau*. Ed. by D. Ter Haar. Pergamon, Jan. 1965, pp. 445–460. ISBN: 978-0-08-010586-4. DOI: [10.1016/B978-0-08-010586-4.50066-3](https://doi.org/10.1016/B978-0-08-010586-4.50066-3).

- [9] A. Arsen'ev. 'Global existence of a weak solution of Vlasov's system of equations'. In: *USSR Computational Mathematics and Mathematical Physics* 15.1 (1975), pp. 131–143. ISSN: 0041–5553. DOI: [10.1016/0041-5553\(75\)90141-X](https://doi.org/10.1016/0041-5553(75)90141-X).
- [10] A. Arsen'ev. 'Existence and uniqueness of the classical solution of Vlasov's system of equations'. In: *Zhurnal Vychislitelnoi Matematiki i Matematicheskoi Fiziki* 15 (Oct. 1975), pp. 1344–1349.
- [11] S. Ukai and T. Okabe. 'On classical solutions in the large in time of two-dimensional Vlasov's equation'. In: *Osaka Journal of Mathematics* 15.2 (Jan. 1978), pp. 245–261. ISSN: 0030-6126.
- [12] K. Pfaffelmoser. 'Global classical solutions of the Vlasov–Poisson system in three dimensions for general initial data'. In: *Journal of Differential Equations* 95.2 (Feb. 1992), pp. 281–303. ISSN: 0022–0396. DOI: [10.1016/0022-0396\(92\)90033-J](https://doi.org/10.1016/0022-0396(92)90033-J).
- [13] P. Lions and B. Perthame. 'Propagation of moments and regularity for the 3-dimensional Vlasov–Poisson system'. In: *Inventiones mathematicae* 105.1 (Dec. 1991), pp. 415–430. ISSN: 1432–1297. DOI: [10.1007/BF01232273](https://doi.org/10.1007/BF01232273).
- [14] C. Mouhot and C. Villani. 'On Landau damping'. In: *Acta Mathematica* 207.1 (2011), pp. 29–201. ISSN: 0001-5962. DOI: [10.1007/s11511-011-0068-9](https://doi.org/10.1007/s11511-011-0068-9).
- [15] C. Birdsall and A. Langdon. *Plasma Physics via Computer Simulation*. Series in Plasma Physics. Taylor & Francis, 2004. ISBN: 978-1-4822-6306-0.
- [16] R. Glassey. *The Cauchy Problem in Kinetic Theory*. Society for Industrial and Applied Mathematics, Jan. 1996. ISBN: 978-0-89871-367-1. DOI: [10.1137/1.9781611971477](https://doi.org/10.1137/1.9781611971477).
- [17] L. Rosenhead. 'The Formation of Vortices from a Surface of Discontinuity'. In: *Proceedings of the Royal Society of London* 142.832 (Nov. 1931), pp. 170–192.
- [18] F. Harlow. 'Hydrodynamic Problems involving large Fluid distortions'. In: *Journal of the Association of computing machinery* 4 (Apr. 1954), pp. 137–142. ISSN: 0004–5411. DOI: [10.1145/320868.320871](https://doi.org/10.1145/320868.320871).
- [19] M. Evans and F. Harlow. 'The Particle-In-Cell method for Hydrodynamic Calculations'. In: *Report LA-2139, Los Alamos Scientific laboratory of the university of California* (1957).
- [20] G.-H. Cottet and P.-A. Raviart. 'Particle Methods for the One-Dimensional Vlasov–Poisson Equations'. In: *SIAM Journal on Numerical Analysis* 21.1 (June 1984), pp. 52–76. ISSN: 0036–1429. DOI: [10.1137/0721003](https://doi.org/10.1137/0721003).
- [21] R. Hockney and J. Eastwood. *Computer Simulation Using Particles*. CRC Press, Mar. 2021. ISBN: 978-1-4398-2205-0.
- [22] A. Myers, P. Colella and B. Straalen. 'A 4th-Order Particle-in-Cell Method with Phase-Space Remapping for the Vlasov–Poisson Equation'. In: *SIAM Journal on Scientific Computing* 39.9 (Feb. 2016), B467–B485. ISSN: 1095–7197. DOI: [10.1137/16M105962X](https://doi.org/10.1137/16M105962X).
- [23] N. Besse and E. Sonnendrücker. 'Semi-Lagrangian schemes for the Vlasov equation on an unstructured mesh of phase space'. In: *Journal of Computational Physics* 191.2 (2003-11), pp. 341–376. ISSN: 0021–9991. DOI: [10.1016/S0021-9991\(03\)00318-8](https://doi.org/10.1016/S0021-9991(03)00318-8).
- [24] F. Charles, B. Després and M. Mehrenberger. 'Enhanced Convergence Estimates for Semi-Lagrangian Schemes Application to the Vlasov–Poisson Equation'. In: *SIAM Journal on Numerical Analysis* 51.2 (Jan. 2013), pp. 840–863. ISSN: 0036–1429. DOI: [10.1137/110851511](https://doi.org/10.1137/110851511).
- [25] J. A. Rossmannith and D. C. Seal. 'A positivity-preserving high-order semi-Lagrangian discontinuous Galerkin scheme for the Vlasov–Poisson equations'. In: *Journal of Computational Physics* 230.16 (2011), pp. 6203–6232. ISSN: 0021–9991. DOI: [doi.org/10.1016/j.jcp.2011.04.018](https://doi.org/10.1016/j.jcp.2011.04.018).
- [26] H. Wendland. *Scattered Data Approximation*. Cambridge Monographs on Applied and Computational Mathematics. Cambridge University Press, 2004. ISBN: 978-0-521-84335-5. DOI: [10.1017/CB09780511617539](https://doi.org/10.1017/CB09780511617539).
- [27] G. Fasshauer. *Meshfree Approximation Methods with MATLAB*. World Scientific Publishing Co., Inc., 2007. ISBN: 978-981-270-634-8.
- [28] S. De Marchi and R. Schaback. 'Stability of kernel-based interpolation'. In: *Advances in Computational Mathematics* 32.2 (Feb. 2010), pp. 155–161. ISSN: 1572–9044. DOI: [10.1007/s10444-008-9093-4](https://doi.org/10.1007/s10444-008-9093-4).

- [29] C. Rieger. ‘Sampling Inequalities and Applications’. PhD thesis. University of Göttingen, Feb. 2009.
- [30] C. Franke and R. Schaback. ‘Solving partial differential equations by collocation using radial basis functions’. In: *Applied Mathematics and Computation* 93.1 (July 1998), pp. 73–82. ISSN: 0096–3003. DOI: [10.1016/S0096-3003\(97\)10104-7](https://doi.org/10.1016/S0096-3003(97)10104-7).
- [31] J. Behrens and A. Iske. ‘Grid-free adaptive semi-Lagrangian advection using radial basis functions’. In: *Computers & Mathematics with Applications* 43.3 (Feb. 2002), pp. 319–327. ISSN: 0898–1221. DOI: [10.1016/S0898-1221\(01\)00289-9](https://doi.org/10.1016/S0898-1221(01)00289-9).
- [32] A. Iske. ‘Radial basis functions: basics, advanced topics and meshfree methods for transport problems.’ In: *Rendiconti del Seminario Matematico* 61.3 (2003), pp. 247–285. ISSN: 0373–1243.
- [33] D. Hunt. ‘Mesh-free radial basis function methods for advection-dominated diffusion problems’. PhD thesis. University of Leicester, Jan. 2005.
- [34] L. Bonaventura, A. Iske and E. Miglio. ‘Kernel-based vector field reconstruction in computational fluid dynamic models’. In: *International Journal for Numerical Methods in Fluids* 66.6 (2011), pp. 714–729. ISSN: 1097–0363. DOI: [10.1002/flid.2279](https://doi.org/10.1002/flid.2279).
- [35] V. Shankar and G. Wright. ‘Mesh-free Semi-Lagrangian Methods for Transport on a Sphere Using Radial Basis Functions’. In: *Journal of Computational Physics* 366 (Aug. 2018), pp. 170–190. ISSN: 0021–9991. DOI: [10.1016/j.jcp.2018.04.007](https://doi.org/10.1016/j.jcp.2018.04.007).
- [36] W. K. Liu, S. Jun and Y. F. Zhang. ‘Reproducing kernel particle methods’. In: *International Journal for Numerical Methods in Fluids* 20.8 (1995), pp. 1081–1106. ISSN: 1097–0363. DOI: [10.1002/flid.1650200824](https://doi.org/10.1002/flid.1650200824).
- [37] T. Arber and R. Vann. ‘A Critical Comparison of Eulerian-Grid-Based Vlasov Solvers’. In: *Journal of Computational Physics* 180.1 (2002), pp. 339–357. ISSN: 0021–9991. DOI: [10.1006/jcph.2002.7098](https://doi.org/10.1006/jcph.2002.7098).
- [38] M. Mehrenberger, L. Navoret and N. Pham. ‘Recurrence phenomenon for Vlasov–Poisson simulations on regular finite element mesh’. In: *Communications in Computational Physics* (2020). DOI: [10.4208/cicp.0A-2019-0022](https://doi.org/10.4208/cicp.0A-2019-0022).
- [39] H. Abbasi, M. Jenab and H. Pajouh. ‘Preventing the recurrence effect in the Vlasov simulation by randomizing phase-point velocities in phase space’. In: *Phys. Rev. E* 84 (Sept. 2011). DOI: [10.1103/PhysRevE.84.036702](https://doi.org/10.1103/PhysRevE.84.036702).